Supplementary Information

Electrochemical Direct Air Capture with Intermittent Renewable Energy: Techno-economic Insights from Solar-Driven Electrodialysis Systems

Guokun Liu [a], Yukun Zhang [a], Meng Lin [b,*], Aidong Yang [a,*]

[a] Department of Engineering Science, University of Oxford, Oxford OX1 3PJ, UK. E-mail: aidong.yang@eng.ox.ac.uk

[b] Department of Mechanical and Energy, Southern University of Science and Technology, Shenzhen 518055, China. E-mail: linm@sustech.edu.cn

* Corresponding authors

Table of Contents

1. Solution Regeneration 1

2. Mathematical Models of System Components 3

3. Model Validation 7

4. Simulation Operating Logic of Systems 10

5. Effect of Repetitive BPM Unit Number in Single Cells 12

6. Method of Economic Calculation 13

7. Variation Coefficient of Daily Solar Irradiance 15

8. Regional Solar Irradiance and DAC Cost Data for China and the UK 16

9. Grid-Assisted Electricity Supply 18

10. Levelized Cost of PV Electricity 19

11. Reported Performance of DAC Systems 20

12. Electrochemical Cells for CO_2 Capture 21

13. Sensitivity Analysis of Electrochemical Cells 22

References 22

1. Solution Regeneration

The carbonate/bicarbonate reactions and corresponding equilibrium constants in the regenerative solution are expressed as[1]:

$$CO_3^{2-} + H_2O \; f \quad HCO_3^- + OH^-, \; K_1 = \frac{\left[HCO_3^-\right]\left[OH^-\right]}{\left[CO_3^{2-}\right]} = 10^{-3.67} \; \backslash*$$

MERGEFORMAT (S1)

$$HCO_3^- \; f \quad CO_2(aq) + OH^-, \; K_2 = \frac{\left[OH^-\right]\left[CO_2(aq)\right]}{\left[HCO_3^-\right]} = 10^{-7.65} \; \backslash*$$

MERGEFORMAT (S2)

$$H_2O \; f \quad H^+ + OH^-, \; K_w = \left[H^+\right]\left[OH^-\right] = 10^{-14} \; \backslash*$$

MERGEFORMAT (S3)

$$CO_2(g) \, f \quad CO_2(aq), \; K_h = \frac{\left[CO_2(aq)\right]}{f_{CO_2}} = 10^{-1.47} \; \backslash*$$

MERGEFORMAT (S4)

where f_{CO_2} is the fugacity of CO_2. Assuming the degassing is performed without vacuum and under the condition of atmospheric pressure and 400 ppm CO_2 concentration, it's assumed as 0.0004 atm for the degassed solution equilibrium calculation. The constants are used to calculate the ion concentrations under equilibrium conditions.

Figure S1 illustrates the detailed changes in pH and DIC throughout the solution regeneration cycle. As the solution consists of carbonate/bicarbonate, the pH remains alkaline throughout the loop, even after electrochemical acidification. Acidification and basification occur within the BPMED cells, which operate as a closed system with no DIC change. DIC variations occur during the absorption and degassing processes, while the concentration of metal ions (K^+) remains constant. The governing equation for the cycle can be expressed as:

$$DIC_2 = DIC_3 \qquad \backslash* \text{ MERGEFORMAT (S5)}$$

$$DIC_1 = DIC_4 \qquad \text{* MERGEFORMAT (S6)}$$

$$\left[K^+\right]_1 = \left[K^+\right]_2 \qquad \text{* MERGEFORMAT (S7)}$$

$$\left[K^+\right]_3 = \left[K^+\right]_4 \qquad \text{* MERGEFORMAT (S8)}$$

The ion concentrations of each solution state are primarily determined using equilibrium constants, with particular consideration given to the limitations of CO_2 absorption. Based on estimates of the CO_2 absorption performance of Carbon Engineering's air contactor,[2] the outflow solution exhibits a notable DIC gap compared to the equilibrium (ideal) conditions with the inlet air. The extent of CO_2 absorption can be quantified using the absorption ratio, defined as:

$$R_a = \frac{DIC_2}{DIC_{2,eq}} \qquad \text{* MERGEFORMAT (S9)}$$

where DIC_2 represents the actual DIC after CO_2 absorption (black solid lines), while $DIC_{2,eq}$ is the ideal DIC (red dashed lines) under equilibrium conditions. Under actual operating conditions, the absorption ratio is assumed to be 0.9, which is considered an attainable estimate.[2]

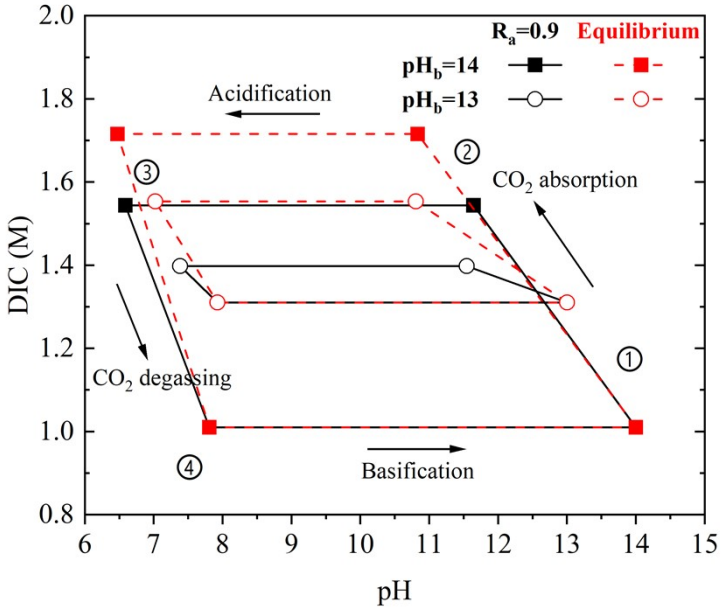

Figure S1. DIC-pH diagram of carbonate/bicarbonate solution regenerative cycle.

The cycles with basified pH values of 13 and 14 are also compared in Figure S1. The

DIC change reflects the DAC capacity of the liquid absorbent. At a basified pH of 13, the DIC change is only 0.1 M, less than half of the equilibrium value, indicating lower absorption efficiency. In contrast, at a basified pH of 14, the actual DIC change reaches approximately 0.5 M, exceeding 70% of the equilibrium value. A higher basified pH and greater pH-swing amplitude enhance both the potential and kinetics of chemical absorption, as well as improve degassing performance. Additionally, a basified pH of 14 closely aligns with the absorbent conditions used in Carbon Engineering's commercial plant, which employs a 1 M KOH solution. This alignment ensures that subsequent cost estimations for the air contactor are more reliable. Therefore, the higher basified pH of 14 has been adopted in this study.

2. Mathematical Models of System Components

2.1 BPMED Cell

The single cell voltage of the BPMED incorporating HER and OER can be expressed as:

$$E_{\text{cell}} = E_{\text{ws}}^{0} + E_{\text{a}} + E_{\text{c}} + E_{\text{BPM}} + E_{\text{ohm}} \text{* MERGEFORMAT (S10)}$$

where E_{ws}^{0} is the standard thermodynamic potential for the water electrolysis reaction, set at 1.229 V under standard temperature conditions. E_{a} and E_{c} a represent the activation overpotentials at the anode and cathode, respectively, and are determined using the Butler-Volmer equation [3]:

$$E_{\text{a}} = \frac{RT}{F} \ln\left(\frac{i}{2i_{0,\text{a}}}\right) \qquad \text{* MERGEFORMAT (S11)}$$

$$E_{\text{c}} = \frac{RT}{F} \ln\left(\frac{i}{2i_{0,\text{c}}}\right) \qquad \text{* MERGEFORMAT (S12)}$$

where $i_{0,\text{a}}$ and $i_{0,\text{c}}$ are the anode and cathode exchange current densities, respectively, set to 0.0048 and 0.19 mA cm^{-2} based on reported values.[3]

The potential of the BPM, E_{BPM}, is primarily determined by the pH difference across the membrane and can be expressed as[4]:

$$E_{\mathrm{BPM}} = n_{\mathrm{BPM}}\left(0.52 + 0.059\Delta pH\right)\backslash^{*}\ \mathrm{MERGEFORMAT} \quad \text{(S13)}$$

where the term 0.52V accounts for the reaction overpotential associated with the BPM's water dissociation process.[5]

The ohmic loss E_{ohm} is determined by the resistance of the solution electrolyte and membranes. It can be expressed as:

$$E_{\mathrm{ohm}} = i\cdot\left[R_{\mathrm{e}} + n_{\mathrm{BPM}}R_{\mathrm{BPM}} + (n_{\mathrm{BPM}}+1)R_{\mathrm{CEM}}\right]\backslash^{*}\ \mathrm{MERGEFORMAT} \quad \text{(S14)}$$

where R_{BPM} and R_{CEM} are the electric resistances of a single BPM and CEM, respectively. In this study, they are set as 10 Ω cm^2 and 4 Ω cm^2, respectively.[4] n_{BPM} is the number of repetitive BPM units in a cell. The resistance of the solution electrolytes R_{e}, considering the effect of gas volumetric fraction φ, can be expressed as[6]:

$$\sigma_{mp} = \sigma\frac{8(2-\varphi)(1-\varphi)}{(4+\varphi)(1-\varphi)} \quad \backslash^{*}\ \mathrm{MERGEFORMAT}\ (\mathrm{S15})$$

$$R_{\mathrm{e}} = \frac{L}{\sigma_{\mathrm{mp}}} \quad \backslash^{*}\ \mathrm{MERGEFORMAT}\ (\mathrm{S16})$$

where σ and σ_{mp} are the conductivity of the pure liquid and multi-phase electrolytes. L is the thickness of the electrolyte compartment.

For the BPMED cell with $K_3/K_4Fe(CN)_6$ redox couple, the single cell voltage is expressed as:

$$E_{\mathrm{cell}} = E_{\mathrm{a}} + E_{\mathrm{c}} + E_{\mathrm{BPM}} + E_{\mathrm{ohm}}\ \backslash^{*}\ \mathrm{MERGEFORMAT}\ (\mathrm{S17})$$

The calculation of each potential follows the methods described above. The electrode exchange current density for the $K_3/K_4Fe(CN)_6$ redox couple set to 229 mA cm^{-2}.[7]

The power consumption of the entire BPMED stack is calculated as the sum of the power consumption of single cells:

$$P_{\mathrm{BPMED}} = n_{\mathrm{cell}} i A_{\mathrm{cell}} E_{\mathrm{cell}} \text{ * MERGEFORMAT (S18)}$$

where n_{cell} is the total number of single cells in the stack, and A_{cell} is the cell effective (single membrane) area.

2.2 Typical-Day Solar Irradiance and PV Power Output

The solar irradiance model is developed to predict the varying PV power conditions over a typical day. This model captures the temporal variation of solar radiation throughout the day, enabling precise simulation of PV power output. Based on Baig et al.'s modified Gaussian distribution function model,[8] the solar radiation intensity is described as follows:

$$r_t = \frac{1}{2\sigma\sqrt{2\pi}}\left[\exp\left(\frac{-(t-12)^2}{2\sigma^2}\right) + \cos\left(\frac{180^\circ(t-12)}{S_0 - 1}\right)\right] \text{ * MERGEFORMAT (S19)}$$

$$\sigma = \frac{1}{r_{t=12}\sqrt{2\pi}} \qquad \text{* MERGEFORMAT (S20)}$$

$$S_0 = \frac{2}{15}\arccos\left(-\tan\varphi \cdot \tan\delta\right) \text{ * MERGEFORMAT (S21)}$$

$$\delta = \arcsin\left(\sin 23.45^\circ \sin\left(\frac{360^\circ(284+n)}{365}\right)\right) \text{ * MERGEFORMAT (S22)}$$

where r_t is the ratio of half-hourly radiation to the day radiation, σ is a constant determined by the noon time value of $r_{\mathrm{t=12}}$, and S_0 is the duration of daylight hours.

The real-time solar radiation intensity can then be calculated by specifying the noon-time radiation intensity $I_{t=12}$:

$$I_{\mathrm{g}} = \frac{I_{t=12}}{r_{t=12}} r_t \qquad \text{* MERGEFORMAT (S23)}$$

The output power of the PV panels is calculated as follows[9]:

$$P_{\mathrm{pv}} = A_{\mathrm{pv}} P_{\mathrm{STC}} \frac{I_{\mathrm{g}}}{I_{\mathrm{STC}}} \left[1 + \alpha_{\mathrm{temp}} \left(T - T_{\mathrm{STC}}\right)\right] \backslash^* \quad \text{MERGEFORMAT (S24)}$$

where P_{STC} is the PV output power at the standard test condition (1000 W m^{-2}, 298 K), which is 188 W in this study.[10] α_{temp} is the temperature coefficient, assumed as -0.39% K^{-1}.[10] The real-time variation of solar radiation and PV power can be determined for any given location and day.

2.3 PEMFC, Electrolyzer, and Hydrogen Storage

The electrolyzer is used to convert surplus PV electricity into hydrogen energy for storage. The stored hydrogen is then utilized by the PEMFC system to sustain BPMED operation during periods of insufficient direct PV power. The power of the electrolyzer and PEMFC is calculated based on the power gap between the PV plant and the BPMED stack:

$$P_{\mathrm{PEMFC}} = \max\left(0, P_{\mathrm{BPMED}} - P_{\mathrm{PV}}\right) \backslash^* \text{ MERGEFORMAT (S25)}$$

$$P_{\mathrm{EL}} = \max\left(0, P_{\mathrm{PV}} - P_{\mathrm{BPMED}}\right) \backslash^* \text{ MERGEFORMAT (S26)}$$

Assuming constant energy efficiencies for both the electrolyzer and PEMFC, the hydrogen generation and consumption rates are expressed as:

$$q_{\mathrm{H_2,g}} = \frac{\eta_{\mathrm{EL}} P_{\mathrm{EL}}}{HHV_{\mathrm{H_2}}} \qquad \backslash^* \text{ MERGEFORMAT (S27)}$$

$$q_{\mathrm{H_2,c}} = \frac{P_{\mathrm{PEMFC}}}{\eta_{\mathrm{PEMFC}} HHV_{\mathrm{H_2}}} \qquad \backslash^* \text{ MERGEFORMAT (S28)}$$

where $HHV_{\mathrm{H_2}}$ is the high heating value of hydrogen. The electrolyzer and PMEFC efficiencies (η_{EL} and η_{PEMFC}) are assumed to be 80%[11] and 50%[12], respectively.

In the BPMED-PEMFC system, the hydrogen generation rate is derived from the BPMED current density as:

$$q_{\mathrm{H_2,g}} = \frac{n_{\mathrm{cell}} i A_{\mathrm{cell}}}{2F} \quad \backslash* \text{ MERGEFORMAT (S29)}$$

Discretizing the simulated system operation period and assuming stable state of each time point, the real-time hydrogen storage amount is expressed as:

$$m_{\mathrm{H_2},t+1} = m_{\mathrm{H_2},t} + \left(q_{\mathrm{H_2,g}} - q_{\mathrm{H_2,c}}\right)\Delta t \backslash* \quad \text{MERGEFORMAT (S30)}$$

The system's required hydrogen storage capacity is determined by the difference between the maximum and minimum hydrogen storage levels:

$$C_{\mathrm{H_2}} = \max\left(m_{\mathrm{H_2},t}\right) - \min\left(m_{\mathrm{H_2},t}\right) \backslash* \quad \text{MERGEFORMAT (S31)}$$

2.4 Battery Storage

A constant efficiency assumption is also applied to the battery energy storage system. The real-time battery energy storage amount is expressed as:

$$E_{\mathrm{BS},t+1} = E_{\mathrm{BS},t} + \left(\eta_{\mathrm{c}} P_{\mathrm{c},t} - \frac{P_{\mathrm{d},t}}{\eta_{\mathrm{d}}}\right)\Delta t \backslash* \quad \text{MERGEFORMAT (S32)}$$

The charging efficiency η_{c} (ratio of the amount of energy stored in the battery to the amount of energy input) and discharging efficiency η_{d} (ratio of the useful energy output to the stored energy in the battery) are both assumed to be 95%.[13] The charging and discharging powers bridge the gap between PV power and BPMED power as:

$$P_{\mathrm{charging}} = \max\left(0, P_{\mathrm{PV}} - P_{\mathrm{BPMED}}\right) \backslash* \text{ MERGEFORMAT (S33)}$$

$$P_{\mathrm{discharging}} = \max\left(0, P_{\mathrm{BPMED}} - P_{\mathrm{PV}}\right) \backslash* \quad \text{MERGEFORMAT (S34)}$$

The required battery storage capacity is determined by the difference between the maximum and minimum battery energy levels:

$$C_{\mathrm{BS}} = \max\left(E_{\mathrm{BS},t}\right) - \min\left(E_{\mathrm{BS},t}\right) \backslash* \text{MERGEFORMAT (S35)}$$

3. Model Validation

3.1 Validation of BPMED cell voltage

The experimental data from Castaño et al.[14] was collected to validate the BPMED cell with HER and OER. The cell design in this experiment differs slightly from the simulation design in this study. Specifically, the experimental cell consists of five BPMs and four CEMs, with each compartment having a thickness of 480 μm. An additional BPM was used to sustain the ionic current within the system instead of a CEM.

The solution in the end compartments consisted of 0.5 M K_2SO_4, while the solution supplied to the acidic and basic compartments was K_2CO_3 and $KHCO_3$, providing an overall concentration of 1 M K^+ and 0.6 M DIC. The cell was tested under varying current densities, with the solution flow rate adjusted to maintain a load ratio of 0.9 (defined as the current divided by the K^+ flow rate supplied to the compartments).

The mathematical model established in this study was applied to simulate the cell configuration used in Castaño et al.'s experiment.[14] Figure S2 presents the comparison of the simulation results with the experimental data.

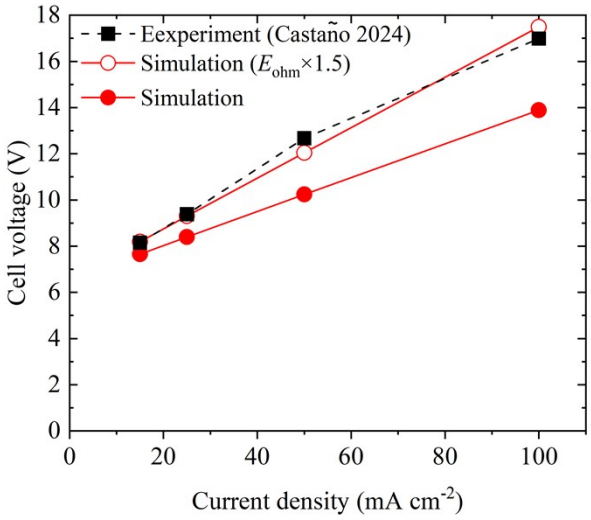

Figure S2. Comparison between experimental and simulated cell voltages of the BPMED with HER and OER.

The measured cell voltage keeps higher than the simulation results, and the gap increase

with the current density. However, both results show a linear increasing trend, implying the increase in cell voltage is dominated by the ohmic loss within the current density range. From Figure S2, the corrected cell voltage with 50% ohmic loss increasing shows the measured cell voltage in the study by Castaño et al.[14] consistently exceeds the simulation results, with the gap increasing as current density rises. However, both datasets exhibit a linear trend, suggesting that the rise in cell voltage is primarily governed by ohmic losses within the current density range tested.

Figure S2 demonstrates that the corrected cell voltage, incorporating a 50% increase in ohmic losses, shows a steeper slope and aligns more closely with the experimental data. The estimated ohmic loss depends on the resistances of the membranes and solutions, which vary considerably based on material selection and cell fabrication processes. This suggests that the simulated cell voltage could be achieved with further optimization of the cell. At lower current densities (10 - 40 mA cm^{-2}), which are the focus of this study, ohmic losses constitute a smaller fraction of the total cell voltage. Consequently, the original simulation results are closer to the experimental data in this range.

For the BPMED cell driven by the $K_3/K_4Fe(CN)_6$ redox reaction, validation was conducted using experimental data from Digdaya et al..[15] Their cell design includes two end compartments for redox reactions and two BPM compartments for the pH swing, separated by two CEMs installed between the acidic/basic compartments and the end compartments. The end compartments and acidic/basic compartments have thicknesses of 5 mm and 2 mm, respectively.

The electrolyte in the end compartments consisted of 0.4 M $K_3/K_4Fe(CN)_6$ solution, while seawater (approximated as 0.5 M NaCl solution with 3.11 M DIC) was supplied to the acidic and basic compartments. The solution flow rate was maintained at 40 mL min^{-1} under various current densities. Figure S3 compares the experimental and simulated cell voltages, showcasing the model's validation results.

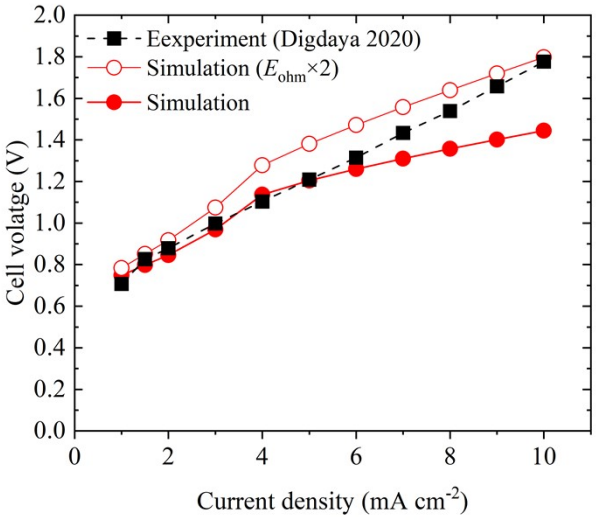

Figure S3. Comparison between experimental and simulated cell voltages of the BPMED with the $K_3/K_4Fe(CN)_6$ redox couple.

The comparison of the redox-couple BPMED cell reveals a similar trend to that observed in the HER/OER cell. The simulated cell voltage closely matches the experimental data, though deviations in the voltage-current slope become apparent at higher current densities. Adjusting the estimation by doubling the ohmic loss provides better alignment with the experimental results. Overall, the error in the simulated cell voltage remains within an acceptable range, indicating that the model captures the key characteristics of the BPMED cell performance effectively.

3.2 Validation of Typical-Day Solar Radiation Intensity

The predicted hourly solar radiation intensity, based on Baig et al.'s model,[8] is compared with open data from the Photovoltaic Geographical Information System (PVGIS). Figure S4 illustrates the comparison results for selected locations and dates.

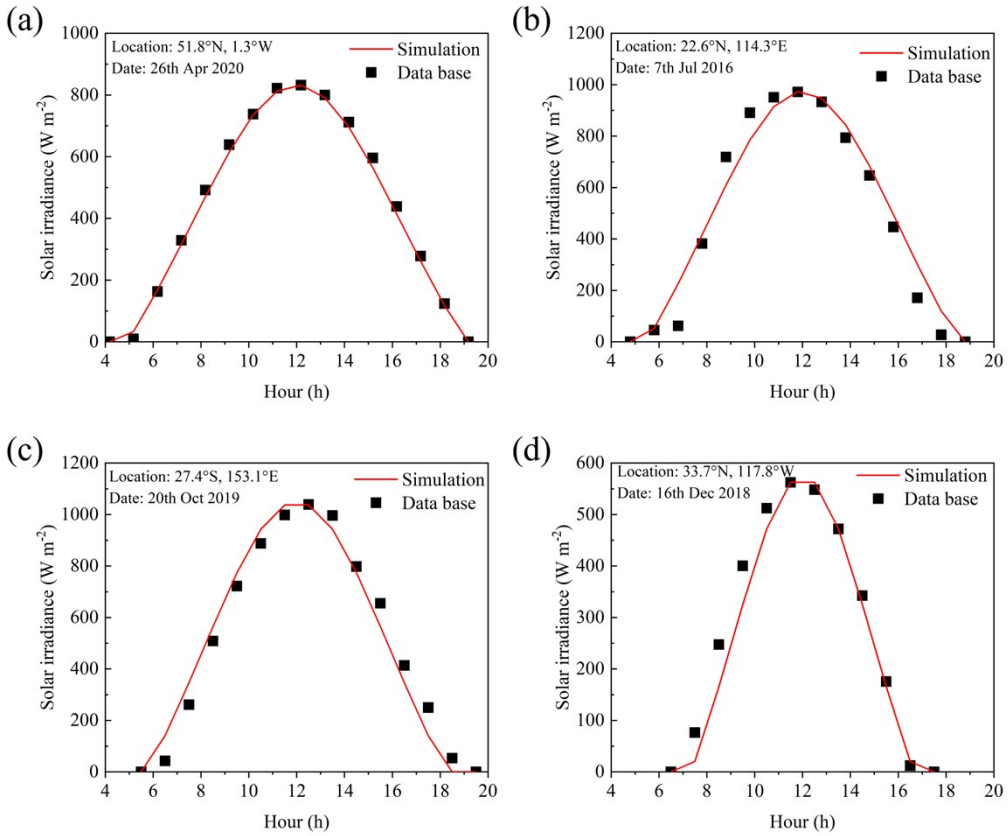

Figure S4. Comparison of daytime solar irradiance between recorded data and model predictions.

The results demonstrate reasonable agreement between the modeled and observed data, validating the reliability of Baig et al.'s model for capturing the diurnal variation in solar radiation intensity across different geographical and temporal conditions. Discrepancies observed in certain instances may be attributed to variations in local atmospheric conditions and the simplified assumptions inherent in the model.

4. Simulation Operating Logic of Systems

The simulation procedure for the systems is depicted in Figure S5. Environmental conditions, including solar irradiance and temperature, along with system parameters, serve as initial inputs. Iterations are performed to determine the appropriate BPMED stack size to ensure the system's overall energy input and consumption are balanced. The systems are entirely driven by renewable solar electricity. This balance is achieved when the energy storage levels at the end of the simulation return to their initial levels, indicating that all solar energy input is fully utilized for DAC without requiring external

energy sources.

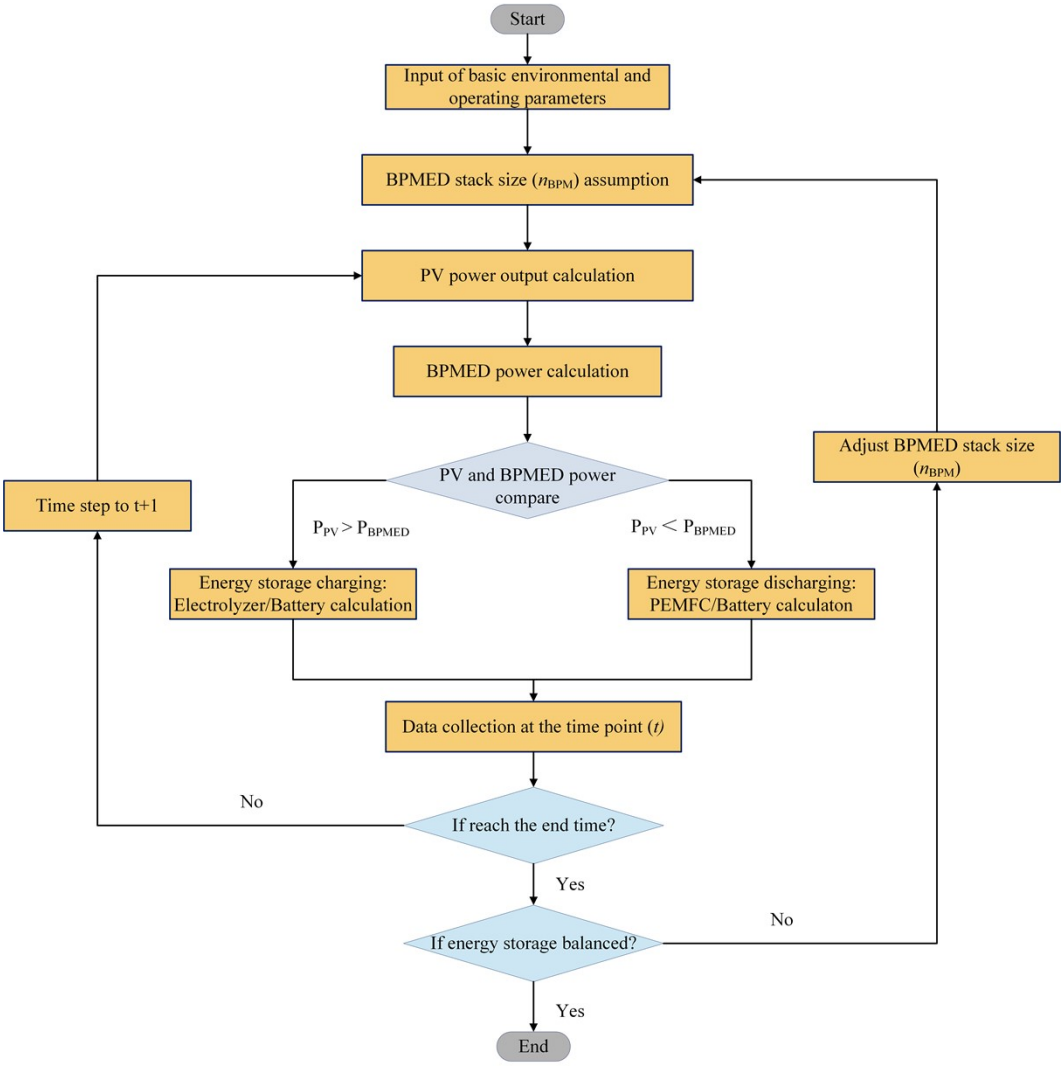

Figure S5. Generalized system simulation flow chart

The entire simulated system operation period is discretized into a series of time intervals (e.g., half an hour or one hour). The system is assumed to operate stably within each interval. The end energy storage amount is compared to the beginning value, and the BPMED stack size is iteratively adjusted to match the overall PV power input. Energy storage systems, including electrolyzers, PEMFCs, and batteries, bridge the power gap between the BPMED and PV outputs.

For the BPMED-PEMFC system, energy storage charging (hydrogen generation) is directly coupled with BPMED operation. In this case, the operating current density adjusts dynamically based on PV direct power input. During periods of low PV input (e.g., nighttime), the PEMFC consumes stored hydrogen to maintain a minimum BPMED operating load and current density. An additional internal iteration is

performed to determine this minimum BPMED current density specific to the BPMED-PEMFC system.

5. Effect of Repetitive BPM Unit Number in Single Cells

The BPMED-PEMFC system was simulated under various configurations with different numbers of single-cell BPMs. Figure S6 compares the BPMED current densities and daily CO_2 capture amounts, with all configurations evaluated under identical PV power input and an average current density of 10 mA cm^{-2} throughout the day.

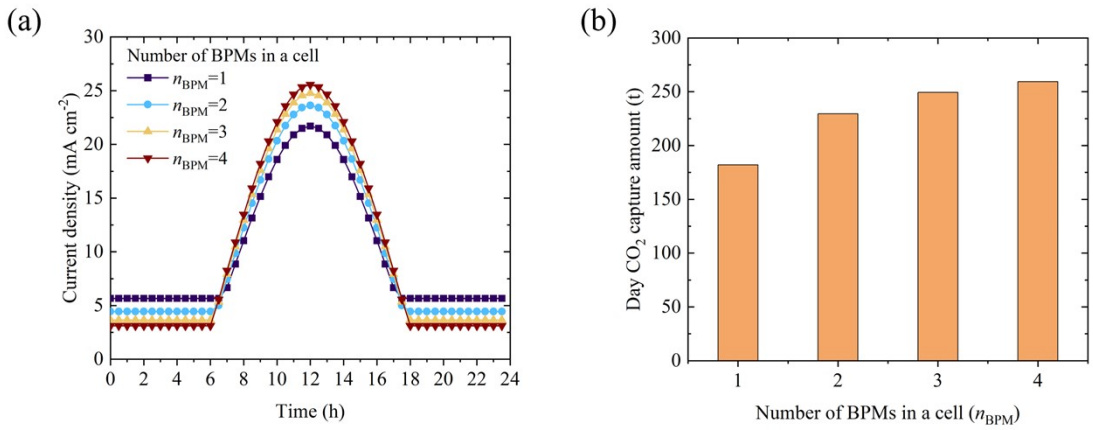

Figure S6. Effect of BPM unit number in HER/OER cells: (a) Current density over the day; (b) System daily DAC capacity.

In all cases, the load of HER/OER cells and the BPMED stack fluctuates with the directly input PV electricity during the daytime, as there is no stand-alone electrolyzer to flexibly absorb excess PV electricity. As the number of BPM units increases, the overall cell voltage and power consumption rise. However, the proportion of energy allocated to HER/OER in the end compartments decreases within the total energy consumption, widening the gap between the available energy during daytime and nighttime. Consequently, the fluctuations in BPMED load and current density throughout the day, shown in Figure S6 (a), become more pronounced with increasing BPM numbers. Conversely, configurations with more BPMs benefit from reduced overall losses in hydrogen generation and utilization, leading to enhanced DAC productivity, as shown in Figure S6 (b). Ultimately, to minimize current density fluctuations and better align with the constant current density of redox-couple cells and

systems, a single BPM unit configuration is chosen for HER/OER cells.

In contrast, systems using redox-couple cells can achieve constant operating loads and current densities. Figure S7 compares the daily CO_2 capture capacity of the BPMED-BS system with varying single-cell BPM numbers.

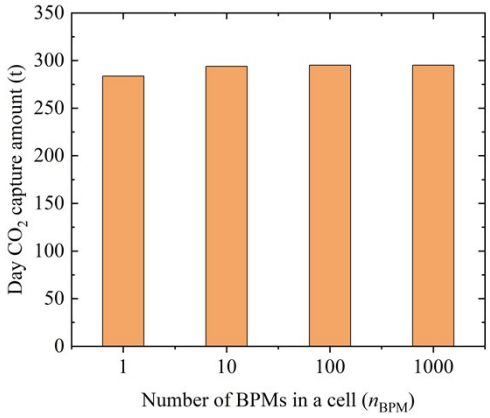

Figure S7. Effect of BPM unit number in redox-couple cells on system DAC performance.

As the number of BPMs in a single cell increases, the potential loss in the end compartments of the redox reaction is distributed across more BPM units, leading to improved energy efficiency and enhanced system DAC performance. However, the gain in daily CO_2 capture becomes negligible beyond 10 BPMs, with only a 0.37% increase observed when the BPM count rises from 10 to 100. This indicates diminishing returns for BPM numbers exceeding 10. Consequently, a configuration with 10 BPM units is selected as the optimal solution for redox-couple cells, balancing energy efficiency and structural simplicity.

6. Method of Economic Calculation

The DAC total cost comprises capital investment and operation and maintenance (O&M) expenses, and is determined using the following equation[6]:

$$TC = \frac{\left(TOC \cdot CCF\right) + C_{\mathrm{O\&M}}^{\mathrm{fix}} + C_{\mathrm{O\&M}}^{\mathrm{var}} h_{\mathrm{eq}}}{R_{\mathrm{CO_2}} h_{\mathrm{eq}}} \text{* MERGEFORMAT} \quad \text{(S36)}$$

where TOC is total overnight cost, CCF is the capital charge factor and assumed as

12.5%,[6] $C_{O\&M}^{fix}$ and $C_{O\&M}^{var}$ are the fixed and variable O&M costs, respectively. R_{CO_2} stands for the total DAC amount in one full year obtained from system simulation. h_{eq} represents the percentage of working hours assumed to be 90%.[6]

Table S1 summarizes the calculation method for the TOC. The TOC is estimated based on the bare erected cost (BEC), which represents the overall costs of purchasing the components and materials listed in

Table S2.

Table S1. Calculation of TOC[6]

Items	Value
Total installation cost (TIC)	80% BEC
Total direct plant cost (TDPC)	BEC + TIC
Indirect cost (IC)	14% TDPC
Engineering, procurement and construction (EPC)	TDPC + IC
Total contingencies and owner's cost (TCOC)	15% EPC
Total overnight cost (TOC)	EPC + TCOC

Table S2. Assumptions of component, material, and other fixed costs

Items	Value
Fixed operation and maintenance costs	
Labor	1.5 M$ [6]
Maintenance	2.5% TOC [6]
Insurance	2.0% TOC [6]
Variable operation and maintenance costs	
CEM	75 $ m^{-2} [6]
BPM	750 $ m^{-2} [6]
CEM & BPM lifetime	3 years [6]
PEMFC	2400 $ kW^{-1} [17]
PEMFC lifetime	5 years [18]
Electrolyzer (alkaline water)	340 $ kW^{-1} [19]
Electrolyzer lifetime	10 years [20]

Energy storage battery	137 \$ kWh^{-1} [21]
Battery lifetime	5 years [22]
Other purchasing costs	
PV panels	63 \$ m^{-2} [21]
BPMED end electrodes	22 \$ m^{-2} [23]
Hydrogen storage tank	577 \$ kg^{-1} [24]
Air contactor (scale of 1 Mt-CO_2/year)	114.2 M\$ [25]

The entire plant's lifetime is assumed to be 20 years. The lifetimes of critical components, such as electrodes and PV panels, are sufficient to cover this period, with electrodes lasting up to 20 years[16] and PV panels lasting approximately 25–30 years.[26] Additionally, components such as the hydrogen tank and air contactor are generally not expected to require replacement during the plant's lifetime. Consequently, the costs associated with these components are excluded from the variable operation and maintenance costs.

7. Variation Coefficient of Daily Solar Irradiance

The original hourly solar irradiance data for different locations were obtained from PVGIS and subsequently aggregated into daily values using 24-hour intervals. The annual total solar irradiance at a given location is calculated as:

$$H_y = \sum_{i=1}^{N} H_i \qquad \text{* MERGEFORMAT (S37)}$$

where H_i is the solar irradiance of the *i*-th day, and N is the total number of days in the year. The annual daily average solar irradiance is then defined as:

$$\mu = \frac{1}{N} H_y = \frac{1}{N} \sum_{i=1}^{N} H_i \qquad \text{* MERGEFORMAT (S38)}$$

Standard deviation is a fundamental statistical measure used to quantify the dispersion of daily solar irradiance around its annual mean value. It is calculated as:

$$\sigma = \sqrt{\frac{1}{N-1}\sum_{i=1}^{N}\left(H_i - \mu\right)^2} \quad \text{* MERGEFORMAT (S39)}$$

While the standard deviation reflects the absolute magnitude of daily solar variability, it depends on the scale and units of the data, which limits its applicability for comparing variability across datasets with different magnitudes. To overcome this limitation, the coefficient of variation of daily solar irradiance is introduced as:

$$CV = \frac{\sigma}{\mu} \quad \text{* MERGEFORMAT (S40)}$$

8. Regional Solar Irradiance and DAC Cost Data for China and the UK

The data from the 50 sites in China and the UK used in Figure 5 are summarized as follows:

Table S3. Site data of China

Site number	Longitude (°)	Latitude (°)	DAC total cost ($ t^{-1}-CO_2)	Annual total solar irradiance (kWh m^{-2})	Variation coefficient of daily solar irradiance
1	109.81	19.046	4733.652859	985.27068	0.563559524
2	120.709	22.74	4947.748504	1125.97812	0.463374051
3	108.844	22.902	5698.414985	819.29906	0.709629526
4	104.976	23.629	5773.557251	715.11834	0.759735781
5	113.853	23.629	4277.687372	890.69043	0.600752636
6	121.236	24.591	6827.080622	869.61253	0.646314224
7	100.494	24.911	4687.326204	1189.69785	0.539474984
8	117.721	25.547	4378.849226	924.52735	0.635109179
9	108.524	26.612	7210.474446	540.52742	1.026290411
10	111.129	27.59	6035.139652	691.26489	0.907093951
11	104.185	27.668	5790.486578	649.03168	0.961209284
12	115.26	27.902	4831.709506	881.54996	0.735917083
13	119.918	29.214	4351.798809	844.84553	0.815837799
14	91.002	29.673	2740.034957	1686.93029	0.32667056
15	85.377	29.902	2595.32043	1926.67233	0.275286213
16	98.033	30.812	3383.493338	1630.18901	0.375622359
17	103.043	31.114	5726.634494	675.74372	0.713292253
18	114.557	31.264	3752.520556	930.58274	0.700320157
19	109.019	31.414	5059.121332	759.32249	0.79920564
20	119.83	32.384	4087.691334	950.89958	0.713454964
21	85.201	33.123	2199.500154	1929.76025	0.274457775
22	94.078	33.564	2805.125516	1635.01265	0.375659863
23	107.086	33.564	4496.610225	853.09005	0.764086302
24	89.288	33.82	2520.510411	1834.44145	0.30518694
25	112.183	34.002	4010.455272	980.73091	0.666346237

26	99.879	34.293	3283.412502	1371.78858	0.47851309
27	117.193	34.655	3850.561861	1082.86411	0.60808108
28	81.422	36.089	2257.731144	1737.18591	0.314434539
29	116.842	37.287	3323.270755	1250.1121	0.48123101
30	93.99	37.426	2364.941868	1903.48352	0.287737519
31	101.9	37.983	2869.514267	1430.71686	0.412191252
32	109.635	38.466	3018.832291	1431.5115	0.434172364
33	87.223	38.535	2597.192452	1766.81959	0.303079509
34	105.711	38.535	2841.70145	1561.3341	0.365958615
35	79.137	39.423	2586.136779	1677.97379	0.322786066
36	116.578	40.568	3103.619251	1309.55703	0.426211264
37	87.223	41.1	2708.950223	1737.59715	0.282280138
38	107.701	41.496	2571.625687	1559.65411	0.327828948
39	122.73	41.496	3052.694684	1325.42662	0.452044607
40	98.912	41.627	2485.860037	1711.51288	0.291605795
41	112.008	42.605	2584.625159	1505.70588	0.342552802
42	91.09	42.67	2445.491382	1754.62476	0.26095949
43	125.982	42.799	3447.189821	1195.47774	0.523467307
44	84.146	43.886	2845.61635	1489.39176	0.419064951
45	130.113	44.953	3302.073156	1178.68035	0.507999649
46	116.666	45.139	2660.356906	1382.909	0.381000577
47	87.223	47.327	4167.574253	1466.42017	0.442607099
48	120.885	47.327	3307.750557	1263.04956	0.45800515
49	127.213	47.92	3599.283165	1225.56131	0.513149636
50	123.258	52.526	4546.812179	1169.36562	0.544894293

Table S4. Site data of the UK

Site number	Longitude (°)	Latitude (°)	DAC total cost ($ t^{-1}-CO_2)	Annual total solar irradiance (kWh m^{-2})	Variation coefficient of daily solar irradiance
1	-4.965	50.367	5934.359526	838.04843	0.743999523
2	-3.891	50.739	5989.158359	881.0781	0.716845793
3	-3.012	50.94	6263.303135	825.957	0.76187912
4	-2.108	50.955	6094.681362	861.05971	0.732130214
5	-0.302	51.047	6335.949605	879.43412	0.721646613
6	0.675	51.185	6309.531568	974.64142	0.681740865
7	-1.278	51.201	6065.46742	834.85333	0.74680013
8	-1.464	51.46	6839.103761	650.7384	0.973330054
9	0.187	51.582	6441.963987	825.70782	0.731790426
10	-2.67	51.778	6478.622124	708.7764	0.831455203
11	-2.123	51.824	8036.692198	575.17503	1.087336071
12	-4.281	51.854	6325.389444	852.14801	0.764207101
13	-0.375	51.914	6533.101292	753.11677	0.779336297
14	-1.571	51.929	6141.962254	735.70157	0.805593381
15	0.431	51.959	6434.163106	832.29614	0.72529659
16	-1.244	52.304	6425.946318	644.57533	0.956065103
17	-3.622	52.379	6522.876875	702.11332	0.870701088
18	-0.229	52.423	6294.768844	780.4598	0.757275065

19	0.724	52.423	6525.353614	810.66725	0.733949984
20	-2.06	52.512	6259.076215	728.4711	0.816054703
21	-0.131	52.72	6263.92679	784.79787	0.75090047
22	-3.573	52.927	7095.181178	676.15674	0.906669504
23	-1.389	53.12	6838.052455	595.07526	1.014890332
24	-0.497	53.147	6229.229208	773.50225	0.760057948
25	-2.499	53.468	6494.81585	736.05002	0.827691114
26	-1.536	53.775	6856.549416	609.16854	1.004445815
27	-0.814	53.844	6260.575054	794.36368	0.748699125
28	-2.523	54.045	7542.850333	723.51214	0.873484812
29	-1.01	54.188	6437.241641	770.6999	0.771702254
30	-6.176	54.331	7840.437021	542.31395	1.076054188
31	-2.073	54.376	10633.58262	468.80248	1.406347236
32	-7.494	54.444	8153.896066	477.03456	1.173207189
33	-2.89	54.501	7843.318519	658.00157	0.939427207
34	-1.645	54.756	6778.482227	753.22718	0.804908253
35	-6.444	54.91	8128.554425	509.26859	1.109920558
36	-3.915	55.022	7014.462492	736.64388	0.854719394
37	-2.283	55.03	7722.791261	560.42292	1.089283312
38	-4.403	55.26	6893.722243	718.15805	0.856095447
39	-3.207	55.371	6773.296193	716.97284	0.849616155
40	-2.182	55.564	7357.306775	754.68367	0.832183425
41	-4.574	56.099	6958.845388	701.89754	0.855871203
42	-3.402	56.371	7567.429367	713.739	0.874237094
43	-4.452	56.667	7844.765808	611.38468	0.977311821
44	-3.134	56.801	7178.817102	733.98905	0.833765083
45	-2.938	57.253	6642.841651	758.3082	0.790998423
46	-4.11	57.292	8812.331565	600.44965	1.012592016
47	-5.282	57.292	9663.892415	534.49378	1.11780315
48	-4.818	57.894	8403.638211	604.56045	0.979919666
49	-6.649	58.178	6731.11556	784.23901	0.820681546
50	-3.793	58.345	7258.177182	765.84186	0.783823131

9. Grid-Assisted Electricity Supply

In grid-assisted operating scenarios, PV electricity remains the primary energy source for BPMED operation. Grid electricity is introduced only when instantaneous PV generation is insufficient to meet the electrical demand required by the BPMED stack and associated subsystems. Grid electricity therefore serves as a supporting or transitional supply, rather than a continuous primary power source. This operating strategy reflects realistic deployment conditions for renewable-powered industrial systems and enables systematic identification of the lower bound of electricity cost under constrained renewable availability.

Two distinct metrics are defined to characterize grid-assisted operation: Grid support

fraction, $f_{\text{grid}}^{\text{support}}$, defined as the fraction of BPMED electrical demand supplied by the grid during time steps when PV generation is insufficient. Annual grid electricity share, φ_{grid}, defined as the ratio of grid-supplied electricity to the total annual electricity consumption of the BPMED system. The grid support fraction is a prescribed operational parameter, whereas the annual grid electricity share emerges as a system-level outcome from time-resolved simulation.

At each simulation time step, the electrical demand of the BPMED system is compared with available PV power. When BPMED demand power is higher than PV output power, the grid power is calculated as:

$$P_{\text{gird}} = f_{\text{grid}}^{\text{support}} \left(P_{\text{BPMED}} - P_{\text{PV}} \right) \quad \text{* MERGEFORMAT (S41)}$$

The remaining demand is met by energy storage where applicable. Over an annual period, the total grid electricity input is integrated to compute annual grid electricity share:

$$\varphi_{\text{gird}} = \frac{\sum P_{\text{grid}}}{\sum P_{\text{BPMED}}} \times 100\% \quad \text{* MERGEFORMAT (S42)}$$

Grid-assisted scenarios represent transitional or hybrid deployment strategies and are not intended to describe fully decarbonized end states. Sensitivity to grid carbon intensity is not explicitly modeled here but does not affect the structural conclusions regarding cost reduction pathways and electricity cost lower bounds.

In the system economic calculations, the price of grid electricity is assumed to be constant at 80 \$ MWh^{-1} to simplify the analysis and enable consistent comparison across different scenarios.

10. Levelized Cost of PV Electricity

Table S5 summarizes recent reports on the levelized cost of electricity (LCOE) from PV power generation. Three primary strategies have emerged to address PV intermittency and enable more competitive LCOEs: integration with complementary energy sources; deployment of advanced energy storage systems; connection to the power grid as a large-scale buffer. Reported LCOEs generally range from 40 to 600 \$ MWh^{-1}, with the majority falling between 50 and 400 \$$MWh^{-1}$. This range can be

considered a representative benchmark for PV-based electricity generation.

Table S5. Summary of LCOEs of PV electricity

Power generation	Energy storage	Off-grid	LCOE ($ MWh^{-1})	Reference
PV	Battery	Yes	160	27
PV	Battery	No	193-273	28
PV and wind	Thermal	Yes	122	29
PV and wind	Battery	Yes	181	29
PV and wind	Hydrogen	Yes	122	29
PV and wind	Thermal	Yes	223	29
PV and wind	Battery, hydrogen, and thermal	Yes	313	30
PV, wind and CSP	Battery and thermal	No	53-160	31
PV and diesel	Battery	Yes	569-595	32
PV and SOFC	N.A.	Yes	40-110	27
PV and natural gas	Liquid air	No	91	33
PV and biogas	Battery	No	280	34

11. Reported Performance of DAC Systems

Table S6 summarizes the reported energy consumption and cost ranges of major commercial and pilot-scale DAC systems. These data represent the most widely cited benchmarks for assessing the techno-economic status of currently deployed or announced DAC technologies.

Table S6. Summary of main deployed DAC technologies, energy consumption, and cost.

Company/Plant	Method	Energy consumption (kJ mol^{-1}-CO_2)	Cost ($ t^{-1}-CO_2)
Carbon Engineering[25,35]	Liquid wet-scrubbing	388 (natural gas)	94-232
Climeworks Orca[35-38]	Solid sorbent-scrubbing	317 (heat and electricity)	500-600
Climeworks 2030 target[a]	Solid sorbent-scrubbing	~159[b]	250-350

Global Thermostat	Solid amine-scrubbing	N.A.	<100[c]

a, Publicly claimed by Climeworks in 2024. b, Estimated as approximately half of the current energy consumption. c, Claimed by Global Thermostat, but not yet validated by publicly disclosed data.

12. Electrochemical Cells for CO_2 Capture

Table S7 summarizes representative electrochemical systems that have been explored for CO_2 capture and release. The four main categories include BPMED, proton-coupled electrolysis, capacitive deionization, and redox-active carrier systems. These approaches differ substantially in reaction mechanisms, operational potentials, and cost-determining components.

Table S7. Overview of electrochemical cells for CO_2 capture.

Electrochemical cells	Voltage range (V)	Energy consumption (kJ mol^{-1}-CO_2)	Key costs
BPMED[a]	1.0-2.4	375-937	Membranes
Proton-coupled electrolysis[39-43]	0.5-2.0	100-300[b]	Electrode, catalyst
Capacitive deionization[44-46]	<1[c]	30-60[b]	Electrode, membrane, current collector
Redox-active carriers[47-49]	0.2-1.2[d]	≈100	Electrode, redox-absorption medium, solvent

a, Simulation results based on Shenzhen case. b, The lower values are normally for rich CO_2 sources (flue gas). c, Operation voltage of charging and discharging. d, Varies significantly among different redox systems.

Overall, these electrochemical pathways offer promising routes for low-temperature, electrically driven carbon capture. However, the actual energy performance depends strongly on CO_2 concentration (e.g., flue gas vs. DAC), system design, and material durability.

13. Sensitivity Analysis of Electrochemical Cells

The baseline values and limits for the evaluated electrochemical DAC systems are summarized in Table S8. The simulations are conducted under the Shenzhen case with a constant electrochemical device load (i.e., fixed current density). Assuming a fixed LCOE of 50 \$ MWh^{-1} and based on Figure 7B, the corresponding optimal current density for the BPMED system is 80 mA cm^{-2}. Accordingly, the baseline values are derived from the BPMED simulation and are listed in Table S8. To account for the potentially wide performance range of other electrochemical technologies, the lower and upper limits of these parameters are defined.

Table S8. Parameters for electrochemical DAC sensitivity analysis.

Parameters	Baseline value	Lower limit	Upper limit
Cell voltage (V)	2.13	0.5	4
Current density (mA cm^{-2})	80	20	100
Current efficiency (%)	52.29	20	80
Cell lifetime (year)	5	1	10
Cell unit area cost (\$ m^{-2})	836.90	100	1000

Here, the current efficiency is defined as the ratio of charge associated with captured CO_2 to the total charge transferred through the cell:

$$\eta_{\mathrm{F}} = \frac{2n_{\mathrm{CO_2}}F}{iA_{\mathrm{cell}}} \times 100\% \qquad \text{* MERGEFORMAT (S43)}$$

where $n_{\mathrm{CO_2}}$ is the DAC rate derived from a single cell/single BPM unit.

The cell unit area cost represents the total material cost required to fabricate a cell of a given area. For example, in the case of BPMED, it is calculated as the sum of the costs of the BPM and the stack-averaged unit costs of the CEM and the electrodes.

References

1. Jiang W, Liu W, Wang Y, Zhao Z, Li Q, Wu Y, et al. Electrochemically Regenerated Amine for CO_2 Capture Driven by a Proton-Coupled Electron Transfer Reaction. Industrial & Engineering Chemistry Research.

2022;61(36):13578–88.
2. Liu G, Yang A, Darton RC. Numerical Modeling and Comparative Analysis of Electrolysis and Electrodialysis Systems for Direct Air Capture. ACS Sustainable Chem Eng. 2024;12(10):3951–65.
3. Hu K, Fang J, Ai X, Huang D, Zhong Z, Yang X, et al. Comparative study of alkaline water electrolysis, proton exchange membrane water electrolysis and solid oxide electrolysis through multiphysics modeling. Applied Energy. 2022;312:118788.
4. Sharifian R, Wagterveld RM, Digdaya IA, Xiang C, Vermaas DA. Electrochemical carbon dioxide capture to close the carbon cycle. Energ Environ Sci. 2021;14(2):781-814.
5. Oener SZ, Foster MJ, Boettcher SW. Accelerating water dissociation in bipolar membranes and for electrocatalysis. Science. 2020;369(6507):1099–103.
6. Sabatino F, Gazzani M, Gallucci F, van Sint Annaland M. Modeling, Optimization, and Techno-Economic Analysis of Bipolar Membrane Electrodialysis for Direct Air Capture Processes. Ind Eng Chem Res. 2022;61(34):12668–79.
7. Silcox R, Bala Chandran R. Demand-side flexibility enables cost savings in a reversible pH-swing electrochemical process for oceanic CO_2 removal. Cell Reports Physical Science. 2024;5(3):101884.
8. Baig A, Akhter P, Muft A. A novel approach to estimate the clear day global radiation. Renewable Energy. 1991;1(1):119-23.
9. Xiang Y, Cai HH, Liu JY, Zhang X. Techno-economic design of energy systems for airport electrification: A hydrogen-solar-storage integrated microgrid solution. Appl Energ. 2021;283:116374.
10. Belsky AA, Glukhanich DY, Carrizosa MJ, Starshaia VV. Analysis of specifications of solar photovoltaic panels. Renewable and Sustainable Energy Reviews. 2022;159:112239.
11. Flamm B, Peter C, Büchi FN, Lygeros J. Electrolyzer modeling and real-time control for optimized production of hydrogen gas. Applied Energy. 2021;281:116031.
12. Wang Y, Pang Y, Xu H, Martinez A, S. Chen K. PEM Fuel cell and electrolysis cell technologies and hydrogen infrastructure development – a review. Energy & Environmental Science. 2022;15(6):2288–328.

13. Vykhodtsev AV, Jang D, Wang Q, Rosehart W, Zareipour H. A review of modelling approaches to characterize lithium-ion battery energy storage systems in techno-economic analyses of power systems. Renewable and Sustainable Energy Reviews. 2022;166:112584.
14. Vallejo Castaño S, Shu Q, Shi M, Blauw R, Loldrup Fosbøl P, Kuntke P, et al. Optimizing alkaline solvent regeneration through bipolar membrane electrodialysis for carbon capture. Chemical Engineering Journal. 2024;488:150870.
15. Digdaya IA, Sullivan I, Lin M, Han L, Cheng WH, Atwater HA, et al. A direct coupled electrochemical system for capture and conversion of CO_2 from oceanwater. Nat Commun. 2020;11(1):4412.
16. Esfandiari N, Aliofkhazraei M, Colli AN, Walsh FC, Cherevko S, Kibler LA, et al. Metal-based cathodes for hydrogen production by alkaline water electrolysis: Review of materials, degradation mechanism, and durability tests. Progress in Materials Science. 2024;144:101254.
17. Zhao J, Cai S, Luo X, Tu Z. Dynamic characteristics and economic analysis of PEMFC-based CCHP systems with different dehumidification solutions. International Journal of Hydrogen Energy. 2022;47(22):11644–57.
18. Guinot B, Champel B, Montignac F, Lemaire E, Vannucci D, Sailler S, et al. Techno-economic study of a PV-hydrogen-battery hybrid system for off-grid power supply: Impact of performances' ageing on optimal system sizing and competitiveness. International Journal of Hydrogen Energy. 2015;40(1):623–32.
19. Jang D, Kim J, Kim D, Han WB, Kang S. Techno-economic analysis and Monte Carlo simulation of green hydrogen production technology through various water electrolysis technologies. Energy Conversion and Management. 2022;258:115499.
20. Lee H, Gu J, Lee B, Cho HS, Lim H. Prognostics and health management of alkaline water electrolyzer: Techno-economic analysis considering replacement moment. Energy and AI. 2023;13:100251.
21. Ramasamy V, Zuboy J, Woodhouse M, O'Shaughnessy E, Feldman D, Desai J, et al. U.S. Solar Photovoltaic System and Energy Storage Cost Benchmarks, With Minimum Sustainable Price Analysis: Q1 2023. National Renewable Energy Laboratory (NREL), Golden, CO (United States).

22. Li L, Wang B, Jiao K, Ni M, Du Q, Liu Y, et al. Comparative techno-economic analysis of large-scale renewable energy storage technologies. Energy and AI. 2023;14:100282.
23. Metzger M, M. Besli M, Kuppan S, Hellstrom S, Kim S, Sebti E, et al. Techno-economic analysis of capacitive and intercalative water deionization. Energy & Environmental Science. 2020;13(6):1544–60.
24. Kalinci Y, Hepbasli A, Dincer I. Techno-economic analysis of a stand-alone hybrid renewable energy system with hydrogen production and storage options. International Journal of Hydrogen Energy. 2015;40(24):7652–64.
25. Keith DW, Holmes G, Angelo DS, Heidel K. A Process for Capturing CO_2 from the Atmosphere. Joule. 2018;2(8):1573–94.
26. Artaş SB, Kocaman E, Bilgiç HH, Tutumlu H, Yağlı H, Yumrutaş R. Why PV panels must be recycled at the end of their economic life span? A case study on recycling together with the global situation. Process Safety and Environmental Protection. 2023;174:63–78.
27. Al-Khori K, Bicer Y, Koç M. Comparative techno-economic assessment of integrated PV-SOFC and PV-Battery hybrid system for natural gas processing plants. Energy. 2021;222:119923.
28. Kosmadakis IE, Elmasides C, Koulinas G, Tsagarakis KP. Energy unit cost assessment of six photovoltaic-battery configurations. Renewable Energy. 2021;173:24–41.
29. He Y, Guo S, Zhou J, Wu F, Huang J, Pei H. The quantitative techno-economic comparisons and multi-objective capacity optimization of wind-photovoltaic hybrid power system considering different energy storage technologies. Energy Conversion and Management. 2021;229:113779.
30. Liu T, Yang Z, Duan Y. Short- and long-duration cooperative energy storage system: Optimizing sizing and comparing rule-based strategies. Energy. 2023;281:128273.
31. Xiao Y, Zou C, Dong M, Chi H, Yan Y, Jiang S. Feasibility study: Economic and technical analysis of optimal configuration and operation of a hybrid CSP/PV/wind power cogeneration system with energy storage. Renewable Energy. 2024;225:120273.
32. Rangel N, Li H, Aristidou P. An optimisation tool for minimising fuel consumption, costs and emissions from Diesel-PV-Battery hybrid microgrids.

Applied Energy. 2023;335:120748.
33. Legrand M, Labajo-Hurtado R, Rodríguez-Antón LM, Doce Y. Price arbitrage optimization of a photovoltaic power plant with liquid air energy storage. Implementation to the Spanish case. Energy. 2022;239:121957.
34. Ennemiri N, Berrada A, Emrani A, Abdelmajid J, El Mrabet R. Optimization of an off-grid PV/biogas/battery hybrid energy system for electrification: A case study in a commercial platform in Morocco. Energy Conversion and Management: X. 2024;21:100508.
35. McQueen N, Gomes KV, McCormick C, Blumanthal K, Pisciotta M, Wilcox J. A review of direct air capture (DAC): scaling up commercial technologies and innovating for the future. Prog Energy. 2021;3(3):032001.
36. Beuttler C, Charles L, Wurzbacher J. The Role of Direct Air Capture in Mitigation of Anthropogenic Greenhouse Gas Emissions. Front Clim. 2019;1:10.
37. Young J, McQueen N, Charalambous C, Foteinis S, Hawrot O, Ojeda M, et al. The cost of direct air capture and storage can be reduced via strategic deployment but is unlikely to fall below stated cost targets. One Earth. 2023;6(7):899–917.
38. Bisotti F, Hoff KA, Mathisen A, Hovland J. Direct Air capture (DAC) deployment: A review of the industrial deployment. Chemical Engineering Science. 2024;283:119416.
39. Liu T, Wang Y, Wu Y, Jiang W, Deng Y, Li Q, et al. Continuous decoupled redox electrochemical CO2 capture. Nat Commun. 2024;15(1):10920.
40. Jin X, Jin S, Li L, Gordon RG, Wang P, Aziz MJ, et al. Direct air capture of CO_2 in an electrochemical hybrid flow cell with a spatially isolated phenazine electrode. Nat Energy. 2025;10(9):1146–54.
41. Zhao F, Deng Y, Li M, Lv C, Aminabhavi TM, Orhan OY, et al. Low-energy electrochemical CO_2-amine desorption driven by the proton-coupled electron transfer reaction (PCET). Chemical Engineering Journal. 2024;495:153217.
42. Zhu P, Wu ZY, Elgazzar A, Dong C, Wi TU, Chen FY, et al. Continuous carbon capture in an electrochemical solid-electrolyte reactor. Nature. 2023;618(7967):959–66.
43. Xu Y, Liu S, Edwards JP, Xiao YC, Zhao Y, Miao RK, et al. Regeneration of direct air CO2 capture liquid via alternating electrocatalysis. Joule.

2023;7(9):2107–17.

44. Legrand L, Schaetzle O, de Kler RCF, Hamelers HVM. Solvent-Free CO_2 Capture Using Membrane Capacitive Deionization. Environ Sci Technol. 2018;52(16):9478–85.
45. Ullah A, Saleem MW, Kim WS. Performance and energy cost evaluation of an integrated NH_3-based CO_2 capture-capacitive deionization process. International Journal of Greenhouse Gas Control. 2017;66:85–96.
46. Legrand L, Shu Q, Tedesco M, Dykstra JE, Hamelers HVM. Role of ion exchange membranes and capacitive electrodes in membrane capacitive deionization (MCDI) for CO_2 capture. Journal of Colloid and Interface Science. 2020;564:478–90.
47. Seo H, Hatton TA. Electrochemical direct air capture of CO_2 using neutral red as reversible redox-active material. Nat Commun. 2023;14(1):313.
48. Massen-Hane M, Diederichsen KM, Hatton TA. Engineering redox-active electrochemically mediated carbon dioxide capture systems. Nat Chem Eng. 2024;1(1):35–44.
49. Seo H, Rahimi M, Hatton TA. Electrochemical Carbon Dioxide Capture and Release with a Redox-Active Amine. J Am Chem Soc. 2022;144(5):2164–70.